Geol. Mag. **148** (*5–6*), *2011, pp. 819–837. © Cambridge University Press 2011*
doi:10.1017/S0016756811000409

Contrasting settings of serpentinite bodies in the northwestern Zagros Suture Zone, Kurdistan Region, Iraq

NABAZ R. H. AZIZ*, KHALID J. A. ASWAD‡ & HEMIN A. KOYI§†

*Department of Geology, College of Science, Sulaimani University, Kurdistan Region, Iraq
‡Department of Geology, College of Science, Mosul University, Iraq
§Department of Earth Sciences, Uppsala University, Uppsala, Sweden

(*Received* 13 October 2010; *accepted* 15 March 2011; *first published online* 11 July 2011)

Abstract – Protrusions and lenses of serpentinite–matrix mélanges occur at several places along the thrust faults of the Zagros Suture Zone. They separate the lower allochthonous thrust sheet, the 'Lower Allochthon' (i.e. Walash–Naopurdan nappe), of Paleocene–Eocene age from sediments of the Arabian platform and the upper thrust sheet of Mesozoic, ophiolite-bearing terranes termed the 'Upper Allochthon' (i.e. Gemo–Qandil nappe). The serpentinite–matrix mélanges occur mostly as stretched bodies (slices) on both sides of the Lower Allochthon (Hero, Halsho and Pushtashan (HHP) and Galalah, Qalander and Rayat (GQR)). Their overall chondrite-normalized rare earth element (REE) patterns form two main groups. Group One exhibits enrichment in the total REEs ($> 1 \times$ chondrite) whereas the Group Two pattern shows depletion (i.e. $< 1 \times$ chondrite). Bulk-rock MORB-normalized profiles of Group Two are almost flat in the MREE–HREE region with flattening profiles in the Gd–Lu range (> 3 times the MORB composition). In comparison with Group One, Group Two has extremely high REE content and displays variable depletions in the moderately incompatible high-field-strength elements (HFSEs) (Zr, Hf, Y) relative to their adjacent REEs. The REEs in the GQR serpentinite–matrix mélanges have a noticeably high LREE content, and a positive Eu anomaly, and their HREE content never reaches more than $1 \times$ chondrite (i.e. < 0.01 to $1 \times$ chondrite). The latter indicates that the hemipelagic sedimentary, melt-like components (i.e. high LREE, U/La, La/Sm and low Ba/Th) control the geochemical peculiarities of this type of serpentinite. The HHP serpentinite–matrix mélanges, however, are either equally divided between the two REE pattern groups (e.g. Hero, Halsho) or inclined towards Group One (e.g. Pushtashan). Contrary to GQR serpentinites, the variation in HHP serpentinite–matrix mélanges spans a compositional spectrum from U/La-rich to more Ba/Th-rich. Such ratio variations reflect the large variation in these two subducted sedimentary components (i.e. carbonate and hemipelagic sediment mix). The obvious differences in the trace element signatures of the GQR and HHP serpentinite–matrix mélanges might be related to plate tectonic parameters such as convergence rate, subduction age and thickness and type of subducted slab. It is more likely that the influx of subducted components to the mantle wedge relied heavily on the composition of the sedimentary inputs. These vary considerably with time from the relatively deepwater hemipelagic sediments (Qulqula Radiolarite Formation) to platform carbonate sediments (Balambo limestone). The trace element signatures of the GQR and HHP serpentinite–matrix mélanges might suggest multi-staging of the allochthonous sheet emplacement on the Arabian platform sediments.

Keywords: serpentinite, Zagros, Kurdistan Region, tectonic, subduction.

1. Introduction

Serpentinites provide an outstanding opportunity to understand the tectonic processes in the Zagros Suture Zone (ZSZ). This zone comprises two thrust sheets formed in the Neo-Tethys Ocean. They were thrust over the Arabian plate in two distinct phases of subduction and collision, during Late Cretaceous and Mio-Pliocene times (Jassim & Buday, 2006), to form the Penjween–Walash sub-zone (Fig. 1). According to Aswad (1999), this zone is subdivided into two allochthonous nappes: Lower and Upper. These nappes are called thrust sheets by Jassim, Suk & Waldhausrova (2006). Many serpentinite bodies referred to as serpentinite imbricates (Jassim, Suk & Waldhausrova, 2006) are exposed along the thrust faults. Field evidence suggests that some of these are not main components of dismembered ophiolite massifs of the Zagros Suture Zone (N. Aziz, unpub. Ph.D. thesis, Sulaimani Univ., 2008). Consequently, the serpentinite bodies are divided into two types: (1) highly sheared serpentinites which occupy the lower contact of the ophiolitic massifs within the Upper Allochthon and (2) serpentinite–matrix mélanges which occur on both sides of the Lower Allochthon (see Mawat cross-section inset in Fig. 1). The first type, which is associated with ophiolites, includes serpentinite broken formation (massive blocks of metabasite enclosed in a matrix of serpentinite schist) of 80–110 Ma (Aziz, Elias & Aswad, 2011). The second type has drastically different petrogenesis, age and regional field relationships, consists of exotic blocks of mixed age (150 and 200 Ma) and has initial epsilon Nd values εNd(i) of down to −30 (Aziz, Elias & Aswad, 2011). The low εNd(i)

†Author for correspondence: Hemin.Koyi@geo.uu.se

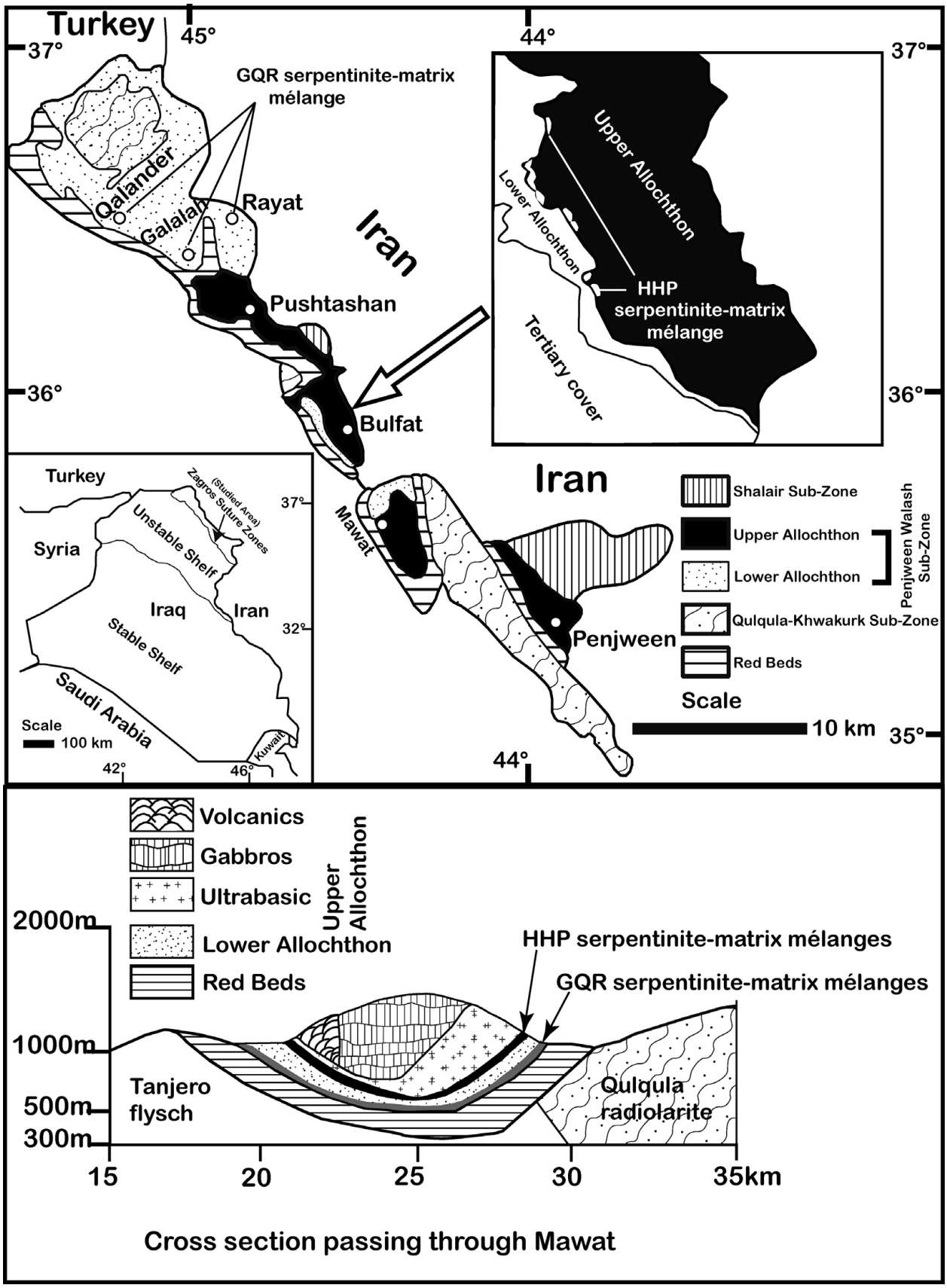

Figure 1. Top: Geological map of the northwestern Zagros Suture Zone (Kurdistan Region) showing the area of the serpentinites studied. Inset – Upper Allochthon with HHP serpentinite–matrix mélanges at base. Bottom: Cross-section passing through Mawat.

https://doi.org/10.1017/S0016756811000409 Published online by Cambridge University Press

values are indicative of maximal incorporation of old crustal rocks into the serpentinite–matrix mélanges. Hence the second type of serpentinite is considered to be a true serpentinite–matrix mélange, occurring mostly on both sides of the Lower Allochthon (Fig. 1). The serpentinite–matrix mélanges occur along thrust faults which superpose the metamorphosed volcano-sedimentary succession of Albian–Cenomanian age (Upper Allochthonous Sheet) onto the underlying unmetamorphosed Tertiary volcano-sedimentary succession (Lower Allochthonous Sheet). Examples are found in the Halsho, Hero and Pushtashan area, referred to as the HHP serpentinite–matrix mélange. They also occur within the lower part of the Tertiary volcano-sedimentary succession (e.g. the Galalah, Qalander and Rayat area) and are thus termed GQR serpentinite–matrix mélanges. Using the above geological and tectonic setting criteria, it is assumed that the GQR and HHP serpentinite–matrix mélanges were emplaced in the late Maastrichtian and the late Palaeogene, respectively.

The present study deals with constraints on petrogenesis and offers a new discussion of the evolution of these two types of serpentinite: serpentinite imbricates and serpentinite–ophiolite associates. Based on field observations, the serpentinite imbricates are interpreted to have been emplaced along the upper and the lower thrust contacts of the Lower Allochthon and are referred to as the HHP and GQR serpentinite–matrix mélanges, respectively. Therefore, special emphasis is placed on the petrogenesis of the GQR and HHP serpentinite–matrix mélanges associated with the two allochthonous thrust sheets mentioned above.

2. Analytical techniques

The sample locations, marked in Figure 1, represent the serpentinite imbricates along the upper and the lower thrust contacts of the Lower Allochthon (Walash volcano-sedimentary series, Paleocene–Eocene). The localities are Halsho, Hero and Pushtashan, and Galalah, Rayat, and Qalander. The serpentinites of the remaining localities (i.e. Penjween, Mawat and Pauza) exhibit highly sheared serpentinites, occupying the lower contact of the ophiolitic massifs. Various analytical techniques were employed for petrographical and geochemical studies. Bulk-rock major, trace and rare earth elements (REEs) were determined at the GeoAnalytical Laboratory, School of Earth and Environmental Science, Washington State University, USA. The major and trace elements were analysed with ThermoARL Advant'XP+ XRF using single low dilution Li-tetraborate fused beads, while REEs were determined with a Sciex Elan 250 inductively coupled plasma-mass spectrometer (ICP-MS) using a combined fusion/dissolution procedure. The chemical compositions of minerals were determined with an electron microprobe technique at the Department of Geology, Uppsala University, Sweden, using a CAMECA SX50 microprobe. The operating conditions were 20 kV accelerating potential and 15 nA beam current. Probe size was normally 1–2 micrometres (serpentine 10 micrometres).

3. Petrography and mineral chemistry

The Zagros Suture Zone serpentinites reveal the relics of original minerals such as olivine, pyroxene and Cr-spinel, and the formation of several metamorphic assemblages. These latter indicate that the original ultramafic protoliths of harzburgite, dunite and to a lesser extent lherzolite, were serpentinized under greenschist to amphibolite facies conditions. The most common textures preserved are pseudomorphic mesh, bastite and hourglass textures after olivine and pyroxene, which preserve the pre-serpentinization textures of the ultramafic precursor (Figs. 2a, b), and non-pseudomorphic (interpenetrating and interlocking) textures. Interpenetrating textures consist of elongated blades of serpentine across previous serpentine generations and textures (Fig. 2c). Interlocking textures, on the other hand, consist of more equigranular grains of serpentine, and may consist of a combination of lizardite, chrysotile and antigorite, especially within the sheared type of serpentinite (Fig. 2d).

Microprobe analysis indicated that the serpentinites contain olivine relics (Fo = 90.6–91.6) and pyroxene relics ($En_{49.25–47.41}$ $Fs_{0.53–5.18}$ $Wo_{50.21–47.41}$), while the metamorphic serpentine group consists of lizardite–chrysotile. The metamorphic serpentine group includes the amphibole types tremolite, actinolite, anthophyllite and paragasite, whereas the chlorite types are clinochlore, penninite and talc-chlorite. The analysis also indicated that the serpentinites contain sulphide, the minerals pyrrohotite ($(Fe_{0.822}$ $Ni_{0.001}$ $Zn_{0.001})_{8.24}$ $S_{1.673}$) and chalcopyrite ($(Cu\ Fe\ Ni)_{0.991}$ $S_{1.591}$), garnet (andradite) ($(Ca_{3.388}$ $Fe_{2.097}$ $Si_{3.163})$ O_{12}) and sphene ($(Ca_{1.029}$ $Ti_{1.073}$ $Si_{0.963})$ O_5). The Cr-spinels show a wide range of Y_{Cr} (Cr/(Cr + Al) atomic ratio) from 0.37 to 1.0, and X_{Mg} (Mg/(Mg + Fe^{2+}) atomic ratio) ranges from 0.0 to 0.75. Three stages, from core to rim, have been recognized in the spinels studied: the residual mantle stage, Cr-rich spinels and a very narrow rim of magnetite. These three stages are represented by primary Cr-spinel, pre-serpentinization spinel and syn- or post-serpentinization spinel, respectively (Fig. 3) (Aswad, Aziz & Koyi, 2011, this issue).

4. Geochemistry

Selected major and trace element variation diagrams were prepared using MgO as the differentiation index (Figs 4, 5). Major element geochemistry shows that the majority of the serpentinite samples indicate ultramafic matrix domains, while a few samples contain < 30 wt % MgO and their values differ considerably from that of the ultramafic protolith (Table 1). In addition, they either form discrete metabasic blocks (serpentinite–ophiolite associates) or are thoroughly mixed with

https://doi.org/10.1017/S0016756811000409 Published online by Cambridge University Press

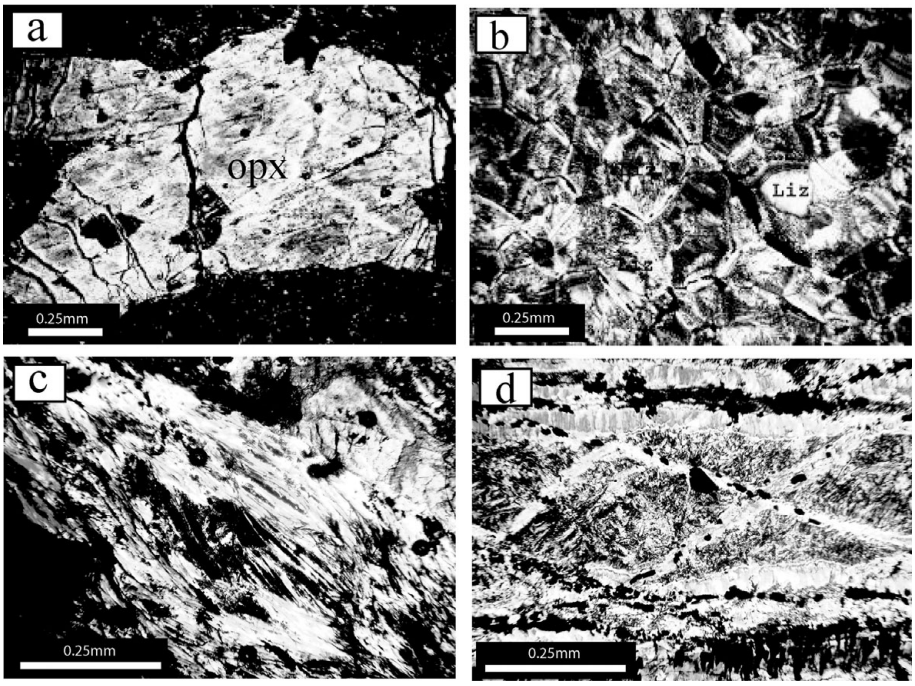

Figure 2. (a) Photomicrograph of mesh texture after olivine. (b) Bastite texture after orthopyroxene. (c) Interpenetrating texture. (d) Interlocking texture.

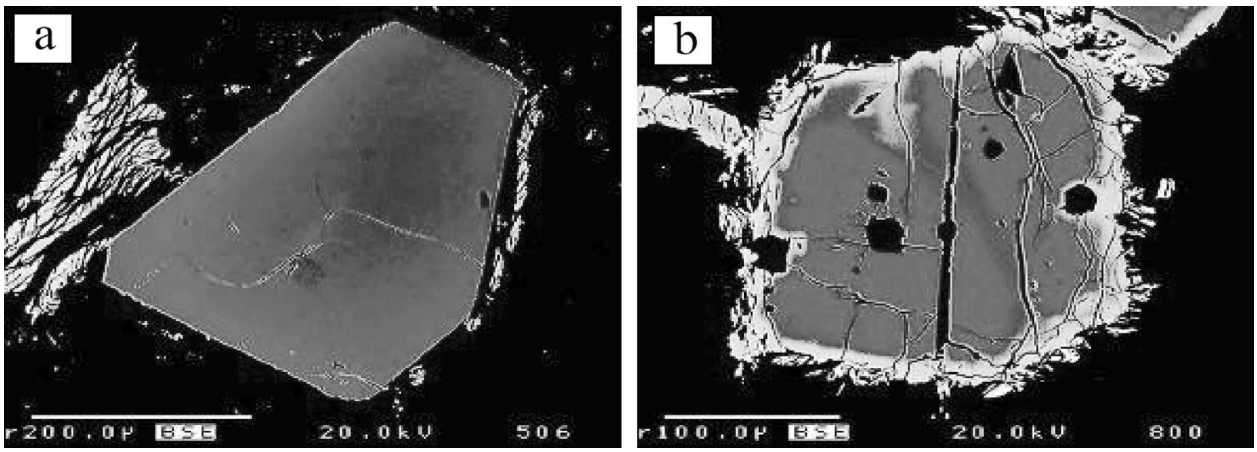

Figure 3. Backscattered image of primary Cr-spinel (a) and Cr-spinel rimmed by magnetite (b).

serpentinite matrix along a mélange channel (typical serpentinite–matrix mélange). Unlike the ophiolite-associated serpentinites (with the exception of Pauza serpentinites, which display high MgO > 30 % as well as low MgO < 10 %), serpentinite–matrix mélanges defy a simple geochemical categorization. On a water-free basis the variation diagrams of MgO versus SiO_2, Al_2O_3, Na_2O and TiO_2 generally display a wide scatter, and the existence of more than one population of cases can be deduced (Fig. 4). Assuming that SiO_2 and Al_2O_3 are both immobile during serpentinization, the mean MgO loss or depletion with respect to SiO_2 is attributed to both metasomatism and variable mechanical mixing between metabasic and metasedimentary blocks and serpentinite matrix processes (Fig. 4). Thus the variation in MgO v. TiO_2 displays a wide scatter and their trends much exceed the corresponding TiO_2 concentrations in ultramafic protoliths, which are represented by the Mawat peridotite (Mirza, unpub. Ph.D. thesis, Sulaimani Univ., Iraq, 2008). The high concentrations of moderately incompatible TiO_2 (> 0.10 %) concomitant with low MgO contents (< 25 %) may indicate that there are considerable subducted components intermixed with serpentinite matrix in the mélange zone. This may be the result of mechanical mixing of serpentinite matrix with SiO_2-rich components (King *et al*. 2006).

In the present analysis, the compatible trace elements of serpentinites are represented by Cr (chromite-compatible element), Ni (olivine-compatible element) and Sc (pyroxene-compatible element). MgO versus Cr and Ni shows coherent trends, demonstrating a compatible trace element character by virtue of their positive correlation with MgO. Sc, however,

https://doi.org/10.1017/S0016756811000409 Published online by Cambridge University Press

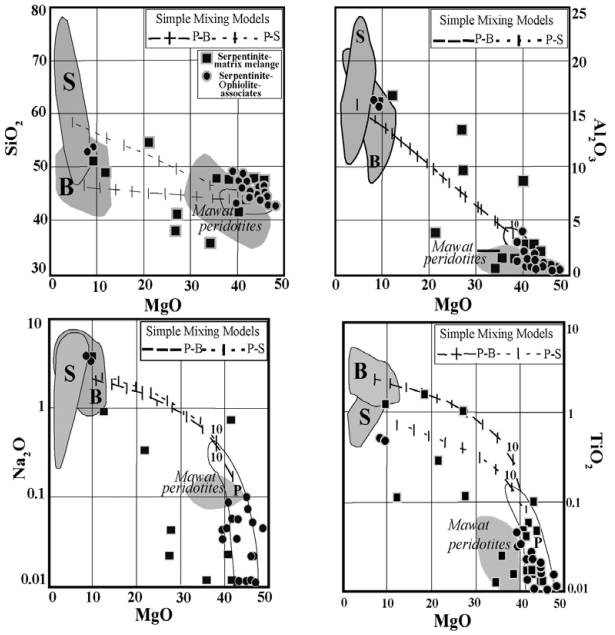

Figure 4. Variation diagrams of MgO (wt %) v. SiO_2, Al_2O_3, TiO_2 and Na_2O for ophiolite–serpentinite associates and ophiolitic mélange serpentinites (all analyses plotted on an anhydrous basis). Mawat peridotites after Mirza (unpub. Ph.D. thesis, Sulaimani Univ., Iraq, 2008). Fields for parental end members are as follows: B and S – basaltic and sedimentary blocks, respectively, all metamorphic grades of the Catalina Schist; P – peridotites of the Horoman Complex, Japan (King *et al*. 2006).

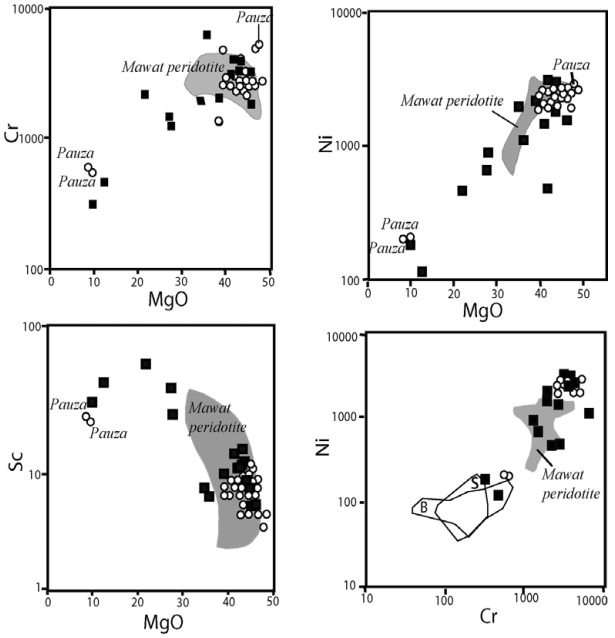

Figure 5. Variation diagrams of MgO (wt %) v. Cr, Ni and Sc for ophiolite–serpentinite associates and ophiolitic mélange serpentinites. Abbreviations as in Figure 4. Note: Pauza samples display high MgO > 40 % as well as low MgO < 10 %, which are not typical mélange serpentinites (i.e. broken formation). (See text for more information.) Mawat peridotite after Mirza (unpub. Ph.D. thesis, Sulaimani Univ., Iraq, 2008).

demonstrates an incompatible trace element character with negative correlation with MgO. In the lherzolite, most of the Cr is contained in Al-chromites and less in clinopyroxene; whereas in the dunite and harzburgite, Cr is contained mainly in Al-chromite (Liu & O'Neill, 2000). Ni is regarded as immobile during metamorphism (Govindaraju, 1995); Sc is geochemically strongly incorporated into pyroxene, which is more abundant in basic blocks. There is much variation in Cr and Ni in the serpentinite–matrix mélange (Fig. 5), while the emphasis on the very low concentration of these compatible elements might indicate that these samples represent variable amounts of mélange blocks (i.e. metabasic and metasediment). Serpentinite–ophiolite associates, however, intermittently contain metabasic blocks (e.g. Pauza, Fig. 5). They are tectonically detached masses of oceanic crust (i.e. broken formation) associated with the thrust mechanism.

4.a. Geochemistry of REEs

The overall chondrite-normalized REE patterns of the Zagros Suture Zone serpentinites studied (Table 2) display significant REE variability, implying that serpentinites of different origins are present. Accordingly, the serpentinites studied fall into two main groups, Group One and Group Two. Their respective REE patterns are shown in Figure 6. The Group One REE pattern displays enrichment in the total REEs of more than 1 × chondrite (CI) (i.e. > 1 × chondrite). In contrast to this, the REE pattern of Group Two (Fig. 6), less than 1 × chondrite (CI) (i.e. < 0.01 to 1 × chondrite), indicates that the mantle protolith composition varies from lherzolite through harzburgite to dunite. This perhaps represents a distinctive boninitic magma of island-arc affinity (fore-arc) related to the suprasubduction zone. The REEs in the GQR serpentinite–matrix mélanges (Fig. 7) have a noticeably positive Eu anomaly, while the heavy REEs (HREEs) never reach more than 1 × chondrite (CI) (i.e. < 0.01 to 1 × chondrite). Because the HREEs are less disturbed, their concentrations should reflect pre-serpentinization partial melting of the mantle wedge much better than light REE (LREE) concentrations do. In the GQR serpentinite–matrix mélanges, however, the LREE and Eu during serpentinization of peridotites must physically reside in highly serpentinized domains. Among all known residual mantle phases (olivine, Opx, Cpx and spinel), Cpx has higher mineral/melt partition coefficients than residual olivine, Opx and spinel (Salters *et al*. 2002). For this reason the progressive partial melting of the mantle wedge is concomitant with decreasing HREE concentrations. Bulk-rock samples also display slightly-to-steeply sloped LREE profiles. As all peridotites are serpentinized to various extents, the elevated abundance of LREEs could be due to serpentinization, a hydrothermal metamorphic process (250–400 °C with up to 13 wt % H_2O in serpentinites), during which the LREEs could be mobile and incorporated (Niu, 2004). The positive Eu anomalies of the

https://doi.org/10.1017/S0016756811000409 Published online by Cambridge University Press

Table 1. Whole-rock major (wt %) and trace (ppm) element analysis of Zagros Suture Zone serpentinites

Sample	Q1	Q2	Q3	Q4	Q5	G1	G2	G3	G4	G5	G6	G7	G8
SiO_2	38.11	40.38	42.65	40.92	38.89	42.40	38.80	28.45	38.52	39.78	38.72	38.33	38.57
TiO_2	0.04	0.02	0.01	0.01	0.01	0.01	0.01	0.01	0.01	0.01	0.02	0.01	0.01
Al_2O_3	2.29	1.19	0.09	0.47	0.63	1.24	0.40	0.32	1.00	0.51	1.82	0.60	0.45
FeO*	4.77	8.99	8.51	4.88	7.94	6.85	8.80	6.65	7.98	7.92	7.45	7.27	8.40
MnO	0.30	0.22	0.11	0.09	0.06	0.10	0.13	0.11	0.15	0.12	0.15	0.10	0.11
MgO	34.88	30.03	37.63	39.15	38.07	34.04	38.47	27.03	37.26	37.69	38.18	39.27	38.55
CaO	2.39	1.59	0.19	0.05	0.08	3.68	0.01	15.37	0.09	0.06	0.03	0.00	0.02
Na_2O	0.65	0.01	0.00	0.01	0.00	0.00	0.00	0.00	0.00	0.00	0.00	0.00	0.00
K_2O	0.04	0.00	0.00	0.00	0.00	0.00	0.00	0.00	0.00	0.00	0.00	0.00	0.00
P_2O_5	0.777	0.007	0.012	0.006	0.004	0.001	0.001	0.010	0.004	0.001	0.001	0.001	0.001
LOI	15.24	15.73	13.67	14.38	13.86	11.53	13.56	21.50	13.59	13.51	13.36	13.98	13.49
Total	99.49	98.17	102.87	99.97	99.54	99.85	100.18	99.45	98.60	99.60	99.73	99.56	99.60
Ni	482	1103	2530	1551	2797	2128	2734	1961	2335	2791	2318	2604	2558
Cr	2731	6302	2978	1898	3292	2053	2766	1967	2846	3196	3117	3241	3084
Sc	14	7	8	6	8	10	8	8	12	8	10	9	7
V	75	99	35	27	30	40	31	39	58	41	56	39	33
Ba	18	49	7	4	1	4	8	0	4	9	5	6	9
Rb	0.84	0.42	0.56	0.70	0.84	1.26	1.40	0.00	0.28	0.70	0.56	0.98	0.84
Sr	733.00	155.00	6.02	1.54	1.40	6.30	0.42	38.00	0.84	3.22	1.26	0.98	0.00
Zr	2.94	2.24	4.06	1.68	2.80	2.38	2.38	1.82	2.24	2.38	2.94	2.66	2.66
Y	23.00	2.94	0.54	0.84	1.12	1.40	0.98	1.40	1.82	0.84	1.12	0.84	0.98
Nb	39.00	0.00	0.83	0.07	0.03	0.03	0.00	0.03	0.00	0.00	0.00	0.00	0.05
Ga	2.24	1.96	1.26	0.14	0.14	4.62	1.54	0.00	1.68	0.00	0.70	1.68	1.12
Cu	8	53	13	10	67	53	6	12	11	30	37	15	45
Zn	16	35	42	24	56	37	48	28	53	39	48	51	36
Pb	0.70	4.06	0.10	0.17	0.00	0.97	0.97	0.05	0.00	0.00	0.00	0.00	0.12
Th	3.37	2.30	0.03	0.09	0.03	0.06	1.53	0.02	1.48	0.99	0.53	1.09	0.07
Hf	–	–	0.06	0.02	0.01	0.02	–	0.01	–	–	–	–	0.02
Ta	–	–	0.03	–	–	–	–	–	–	–	–	–	–
U	–	–	0.01	0.09	0.01	0.03	–	0.08	–	–	–	–	0.03
Cs	–	–	0.00	0.02	0.00	0.36	–	0.01	–	–	–	–	0.01

Table 1. Continued.

Sample	G9	G10	G11	G12	R1	R2	R3	R4	R5	R6	R7	R8
SiO_2	37.94	38.86	38.86	38.79	38.15	39.02	39.14	38.94	38.75	39.23	39.86	37.63
TiO_2	0.108	0.011	0.011	0.010	0.015	0.006	0.005	0.006	0.006	0.007	0.007	0.006
Al_2O_3	8.75	0.94	0.58	0.55	0.63	0.61	0.57	0.60	0.61	0.71	0.59	0.32
FeO*	7.50	7.44	7.98	7.89	10.81	8.63	7.41	7.50	7.06	6.27	6.45	7.77
MnO	0.135	0.139	0.107	0.114	0.061	0.118	0.123	0.109	0.126	0.068	0.054	0.080
MgO	25.10	38.25	38.84	39.07	35.80	37.06	38.09	38.16	37.96	37.96	39.67	37.39
CaO	11.40	0.05	0.02	0.02	0.10	0.18	0.06	0.14	0.57	0.88	0.02	2.43
Na_2O	0.04	0.00	0.00	0.00	0.01	0.00	0.00	0.00	0.00	0.00	0.00	0.00
K_2O	0.00	0.00	0.00	0.00	0.00	0.00	0.00	0.00	0.00	0.00	0.00	0.00
P_2O_5	0.003	0.001	0.002	0.002	0.006	0.005	0.001	0.003	0.001	0.001	0.001	0.001
LOI	8.65	13.51	13.31	13.14	13.20	13.97	13.87	13.96	14.30	14.47	13.53	14.68
Total	99.63	99.20	99.71	99.59	98.78	99.60	99.27	99.42	99.38	99.60	100.18	100.31
Ni	883	2358	2350	2295	3077	2933	2397	2492	2325	2686	2529	2698
Cr	1263	2853	3075	2479	3098	3619	2428	2638	2624	2719	2889	2785
Sc	26	10	9	10	8	10	9	9	9	9	8	5
V	94	47	37	36	35	61	35	37	35	37	40	24
Ba	3	4	6	1	6	6	7	9	6	7	3	2
Rb	0.98	0.70	0.70	0.28	0.00	0.28	1.68	1.26	0.70	0.28	1.26	0.70
Sr	6.02	1.82	0.84	1.12	2.10	2.94	1.40	1.26	5.88	2.38	1.26	39.48
Zr	3.64	2.94	2.24	2.10	3.92	2.94	2.38	1.54	2.38	1.68	1.96	2.80
Y	4.20	1.68	1.26	1.12	1.68	0.84	0.28	0.42	1.12	0.84	0.70	0.98
Nb	0.00	0.00	0.00	0.00	0.00	0.04	0.00	0.00	0.00	0.00	0.02	0.00
Ga	1.26	1.40	0.00	2.10	1.54	0.00	1.54	0.84	0.00	1.96	1.96	0.00
Cu	28	16	72	72	79	23	17	10	5	18	7	7
Zn	30	56	46	41	54	59	50	38	41	53	42	34
Pb	0.00	0.00	0.00	0.00	0.00	0.13	0.00	0.00	0.00	0.00	0.09	0.00
Th	2.45	1.36	1.64	0.76	1.76	0.04	1.50	2.83	2.15	0.72	0.02	1.37
Hf	–	–	–	–	–	0.01	–	–	–	–	0.01	–
Ta	–	–	–	–	–	–	–	–	–	–	–	–
U	–	–	–	–	–	1.22	–	–	–	–	0.02	–
Cs	–	–	–	–	–	0.01	–	–	–	–	0.00	–

Table 1. Continued.

Sample	R9	R10	HS2	HS3	HS4	HS8	HS11	HS12	HS13	HS14	HR16	HR17	HR18	H21	HR25
SiO_2	41.28	39.22	36.09	38.36	46.21	52.58	40.02	39.17	39.17	39.89	39.73	39.91	49.81	39.97	34.42
TiO_2	0.008	0.008	0.042	0.050	0.107	0.285	0.013	0.018	0.015	0.088	0.009	0.011	1.224	0.012	0.936
Al_2O_3	0.50	0.68	7.33	1.11	15.52	3.57	0.96	0.79	0.91	2.33	0.41	0.72	15.55	0.57	11.95
FeO*	4.63	6.99	6.99	9.59	4.08	5.94	8.24	7.56	9.00	6.86	7.76	6.55	9.33	7.05	9.92
MnO	0.118	0.092	0.143	0.106	0.096	0.149	0.084	0.090	0.098	0.121	0.108	0.084	0.139	0.103	0.186
MgO	37.42	39.06	34.85	36.26	11.54	20.69	36.60	37.05	36.40	37.17	38.38	38.15	9.37	39.14	24.28
CaO	1.43	0.08	1.03	0.26	15.65	13.56	0.24	0.82	0.57	0.42	0.25	0.16	6.93	0.32	8.18
Na_2O	0.00	0.00	0.02	0.00	0.90	0.33	0.01	0.00	0.00	0.00	0.00	0.00	4.00	0.01	0.02
K_2O	0.00	0.00	0.00	0.00	0.50	0.05	0.00	0.00	0.00	0.00	0.00	0.00	0.57	0.00	0.00
P_2O_5	0.005	0.006	0.004	0.005	0.002	0.006	0.001	0.003	0.002	0.003	0.004	0.004	0.237	0.003	0.067
LOI	14.40	13.93	13.66	13.28	6.11	3.86	13.80	13.82	13.78	13.33	14.05	13.78	2.89	12.36	10.33
Total	99.79	100.07	100.16	99.02	100.72	101.02	99.97	99.32	99.95	100.21	100.70	99.37	100.05	99.54	100.29
Ni	2411	2355	1457	2498	117	460	2611	2457	2641	1823	2725	2288	182	2387	659
Cr	3100	2797	2652	4014	469	2203	2899	3355	2895	2641	2837	2722	317	2387	1479
Sc	9	8	9	11	42	56	11	11	11	15	6	8	31	8	39
V	38	37	38	50	104	155	43	44	40	59	39	27	194	34	241
Ba	18	5	20	23	109	10	14	19	9	12	13	19	143	4	14
Rb	0.56	0.00	0.42	0.28	9.52	0.56	0.84	0.00	0.70	1.68	0.84	0.70	6.86	0.42	0.84
Sr	6.86	1.82	4.48	3.22	146.16	21.14	3.50	4.34	3.36	3.64	7.28	3.36	423.78	6.02	5.88
Zr	2.94	3.08	4.90	4.48	5.04	9.24	2.52	3.92	2.52	5.32	3.78	3.92	99.96	3.08	45.64
Y	0.98	0.70	2.24	1.68	4.34	6.72	1.26	1.12	0.28	2.80	1.68	1.82	21.14	0.00	21.56
Nb	0.04	0.00	0.02	0.00	0.00	0.05	0.00	0.00	0.00	0.02	0.11	0.00	13.03	0.00	1.18
Ga	2.66	0.70	2.10	1.40	7.42	6.02	0.70	1.54	0.84	1.12	0.84	2.24	15.96	0.84	7.42
Cu	39	6	61	29	63	7	18	20	14	19	8	8	78	6	104
Zn	29	50	47	70	17	60	41	30	50	25	45	39	61	57	62
Pb	0.07	0.00	0.05	0.00	0.00	0.03	0.00	0.00	0.00	0.12	0.12	0.00	1.11	0.00	0.00
Th	3.03	1.69	0.02	1.34	2.18	0.02	1.86	1.16	0.85	0.01	0.03	0.98	1.89	1.08	0.03
Hf	0.01	–	0.04	–	1.12	0.25	–	–	–	0.10	0.01	–	2.40	–	1.45
Ta	–	–	–	–	–	–	–	–	–	–	–	–	0.810	–	0.080
U	0.11	–	0.02	–	–	0.01	–	–	–	0.06	2.71	–	0.57	–	0.01
Cs	0.04	–	0.14	–	–	0.01	–	–	–	0.02	0.02	–	0.35	–	0.15

Table 1. Continued.

Sample	PZ1	PZ2	PZ3	PZ4	PZ5	PZ6	PZ7	PZ8	PZ9	PZ10	M2	M4	M6
SiO_2	42.20	39.06	41.26	40.52	42.32	43.15	40.53	40.90	47.52	48.51	37.70	43.32	45.01
TiO_2	0.009	0.014	0.015	0.009	0.046	0.016	0.008	0.006	0.470	0.440	0.007	0.012	0.029
Al_2O_3	0.42	0.56	0.77	0.49	1.88	0.85	0.23	0.30	14.43	13.95	0.69	0.54	0.92
FeO*	7.27	7.69	7.64	6.82	7.17	7.95	7.69	6.70	5.83	5.90	6.84	7.49	8.35
MnO	0.123	0.117	0.125	0.109	0.095	0.130	0.116	0.083	0.163	0.146	0.186	0.119	0.176
MgO	43.03	43.16	41.24	41.75	36.04	43.09	40.89	39.86	7.56	8.55	35.84	36.78	35.54
CaO	0.50	0.52	0.78	1.01	0.86	0.90	0.35	0.51	9.44	9.20	2.04	0.73	0.32
Na_2O	0.05	0.00	0.07	0.02	0.08	0.10	0.02	0.01	3.50	3.20	0.00	0.00	0.04
K_2O	0.00	0.00	0.01	0.00	0.01	0.00	0.00	0.00	0.57	0.14	0.00	0.00	0.00
P_2O_5	0.003	0.012	0.002	0.004	0.005	0.015	0.008	0.002	0.088	0.088	0.003	0.004	0.014
LOI	6.47	8.91	7.98	9.55	11.08	3.60	10.65	12.48	10.35	9.85	15.33	11.26	9.04
Total	100.08	100.04	99.89	100.28	99.59	99.80	100.49	100.85	99.92	99.97	98.64	100.26	99.44
Ni	2483	2836	2481	2487	1967	2669	2678	2364	198	205	2071	1888	1883
Cr	2637	5208	2546	2501	2627	2966	2754	2563	608	549	2378	2596	4856
Sc	9	4	11	8	9	12	7	7	25	23	9	8	8
V	31	24	45	25	40	46	29	26	158	145	38	28	38
Ba	4	9	4	9	6	11	8	12	101	40	3	35	33
Rb	1.68	0.84	0.14	0.14	0.00	0.98	0.70	0.70	9.52	1.68	0.84	0.28	0.56
Sr	3.36	7.14	4.62	12.88	9.66	3.92	2.94	7.28	211.00	339.0	118.02	24.22	5.46
Zr	3.08	4.06	3.64	3.50	5.88	3.64	1.68	2.80	66.78	68.18	1.68	2.52	3.64
Y	1.26	1.40	0.84	1.82	3.50	1.12	0.70	1.12	12.88	13.58	0.84	1.82	2.10
Nb	0.00	0.21	0.00	0.00	0.14	0.06	0.00	0.00	2.22	1.26	0.00	0.42	0.14
Ga	0.98	1.26	1.40	1.54	4.90	0.98	0.98	0.84	15.26	13.44	1.68	2.38	2.38
Cu	11	80	42	9	15	12	10	6	43	40	45	44	22
Zn	38	63	44	40	57	46	43	38	55	49	63	65	105
Pb	0.00	0.20	0.00	0.00	0.00	0.11	0.00	0.00	1.54	1.26	1.26	0.00	0.00
Th	1.55	0.15	2.85	0.85	2.83	0.06	1.80	1.39	1.09	2.88	1.38	1.32	0.08
Hf	–	0.03	–	–	–	0.01	–	–	2	–	–	–	–
Ta	–	0.01	–	–	–	0.00	–	–	0.15	–	–	–	–
U	–	0.080	–	–	–	0.21	–	–	0.29	–	–	–	–
Cs	–	0.04	–	–	–	0.06	–	–	0.11	–	–	–	–

Table 1. Continued.

Sample	M7	M9	M10	PN1	PN2	PN3	PN4	PN5	PN6	PU1	PU2	PU3	PU4	PU5
SiO_2	41.08	40.91	40.11	39.81	40.54	41.21	38.92	38.73	39.21	40.38	38.19	39.58	37.39	43.20
TiO_2	0.007	0.024	0.009	0.017	0.018	0.007	0.008	0.007	0.005	0.02	0.03	0.02	0.01	0.04
Al_2O_3	0.17	0.57	0.48	0.59	0.46	0.62	0.23	0.44	0.54	1.090	3.440	1.600	0.310	2.530
FeO*	7.88	7.63	7.42	7.19	6.62	7.75	7.92	6.89	8.20	9.98	9.19	7.99	6.60	7.28
MnO	0.150	0.083	0.108	0.102	0.089	0.126	0.123	0.086	0.085	0.11	0.12	0.09	0.12	0.06
MgO	38.14	36.62	37.40	38.40	38.61	41.84	42.22	37.06	38.25	36.05	35.19	37.05	41.86	34.29
CaO	0.21	0.28	0.86	0.03	0.05	1.23	1.43	2.73	0.06	0.03	2.21	0.48	0.20	0.45
Na_2O	0.00	0.03	0.01	0.01	0.01	0.01	0.01	0.01	0.00	0.05	0.04	0.05	0.04	0.03
K_2O	0.00	0.01	0.00	0.00	0.00	0.00	0.00	0.00	0.00	0.01	0.02	0.01	0.02	0.01
P_2O_5	0.002	0.008	0.003	0.003	0.002	0.000	0.000	0.002	0.003	0.04	0.04	0.03	0.03	0.02
LOI	11.97	13.65	13.12	13.80	13.28	7.42	9.50	13.50	13.76	12.80	12.10	13.25	13.20	12.60
Total	99.61	99.82	99.52	99.95	99.68	100.21	100.36	99.46	100.11	100.56	100.57	100.15	99.78	100.51
Ni	1933	2417	2301	2507	2341	2516	1915	2324	2705	2530	2544	2698	2636	2364
Cr	4171	2358	2609	2710	2091	2529	4884	2783	3234	2978	2940	2785	2775	2563
Sc	6	7	10	7	5	9	5	8	10	8	7	5	5	7
V	26	42	35	31	22	38	24	33	43	35	34	24	25	26
Ba	12	14	13	13	14	4	7	8	2	7	5	2	3	12
Rb	0.70	0.84	0.42	1.54	0.28	0.28	2.66	0.42	1.12	0.56	0.98	0.70	1.40	0.70
Sr	6.02	6.44	11.76	1.96	6.30	20.02	75.18	17.08	0.98	6.02	4.90	39.48	39.90	7.28
Zr	1.96	4.20	3.08	2.52	3.08	2.52	2.66	2.10	2.52	4.06	3.50	2.80	3.92	2.80
Y	0.70	1.26	1.82	0.42	1.82	0.70	0.98	0.56	1.82	1.12	1.54	0.98	2.10	1.12
Nb	0.00	0.00	0.00	0.00	0.00	0.00	0.00	0.14	0.00	0.00	0.14	0.00	0.00	0.00
Ga	0.56	0.56	0.28	2.24	1.12	0.42	0.00	0.28	0.70	1.26	2.52	0.00	0.14	0.84
Cu	23	26	10	13	8	20	7	4	6	13	15	7	8	6
Zn	79	53	46	41	36	38	41	41	36	42	42	34	34	38
Pb	0.00	0.00	0.00	0.00	0.00	0.00	0.00	0.00	0.00	0.00	0.00	0.00	0.00	0.00
Th	1.27	1.11	1.92	1.45	0.85	0.76	1.36	0.69	0.97	1.82	2.04	1.37	3.01	1.39
Hf	–	–	–	–	–	–	–	–	–	0.07	–	0.04	–	0.10
Ta	–	–	–	–	–	–	–	–	–	0.03	–	0.02	–	0.01
U	–	–	–	–	–	–	–	–	–	1.05	–	1.09	–	2.05
Cs	–	–	–	–	–	–	–	–	–	0.35	–	0.40	–	0.20

Table 2. Whole-rock REE analysis of Zagros Suture Zone serpentinites

Sample	Q3	Q4	Q5	G1	G3	G8	R2	R7	R9	HS2	HS8
La	6.51	0.22	0.06	0.13	0.05	0.11	0.06	0.03	0.09	0.07	0.20
Ce	5.26	0.45	0.11	0.25	0.09	0.25	0.12	0.08	0.12	0.22	0.68
Pr	0.39	0.05	0.01	0.03	0.01	0.03	0.01	0.01	0.02	0.03	0.15
Nd	1.04	0.22	0.06	0.11	0.04	0.08	0.05	0.03	0.07	0.15	1.00
Sm	0.15	0.05	0.01	0.03	0.01	0.02	0.01	0.00	0.01	0.06	0.52
Eu	0.45	0.02	0.00	0.07	0.00	0.00	0.00	0.00	0.00	0.04	0.14
Gd	0.12	0.05	0.01	0.03	0.01	0.01	0.01	0.01	0.02	0.10	0.85
Tb	0.02	0.01	0.00	0.01	0.00	0.00	0.00	0.00	0.00	0.02	0.16
Dy	0.10	0.05	0.01	0.06	0.01	0.02	0.01	0.00	0.01	0.15	1.05
Ho	0.02	0.01	0.00	0.01	0.00	0.01	0.00	0.00	0.00	0.04	0.22
Er	0.06	0.04	0.02	0.05	0.01	0.02	0.01	0.01	0.02	0.11	0.58
Tm	0.01	0.01	0.00	0.01	0.00	0.00	0.00	0.00	0.00	0.02	0.08
Yb	0.06	0.04	0.03	0.07	0.02	0.03	0.02	0.02	0.04	0.09	0.45
Lu	0.01	0.01	0.01	0.01	0.00	0.01	0.01	0.01	0.01	0.02	0.07

Sample	SH14	HR16	HR18	HR25	PZ2	PZ6	PZ9	PU63	PU65	PU67	M7	PN1
La	0.14	0.13	12.96	1.93	0.22	0.20	6.21	2.80	6.85	2.15	7.97	4.00
Ce	0.73	0.27	26.28	6.87	0.36	0.23	13.42	7.28	12.55	5.25	19.00	10.30
Pr	0.03	0.02	3.39	1.26	0.04	0.03	1.80	2.15	2.44	0.70	2.60	1.50
Nd	0.15	0.09	14.44	7.00	0.15	0.12	7.87	8.75	11.00	6.45	12.50	8.00
Sm	0.09	0.02	3.64	2.41	0.03	0.03	2.01	2.35	3.15	1.87	3.20	2.50
Eu	0.03	0.01	1.32	0.93	0.01	0.01	0.77	0.90	0.95	0.80	1.13	1.12
Gd	0.16	0.02	3.86	3.07	0.03	0.02	2.15	3.52	4.37	2.55	3.20	2.80
Tb	0.05	0.00	0.64	0.59	0.00	0.00	0.36	0.90	0.65	0.30	0.61	0.60
Dy	0.35	0.01	3.94	3.99	0.03	0.04	2.27	3.75	4.15	2.30	3.90	3.90
Ho	0.08	0.00	0.79	0.81	0.01	0.01	0.46	0.58	0.40	0.18	0.85	0.80
Er	0.24	0.02	2.11	2.29	0.02	0.04	1.31	2.31	2.88	1.75	2.20	2.30
Tm	0.04	0.00	0.30	0.33	0.00	0.01	0.18	0.40	0.43	0.30	0.40	0.40
Yb	0.27	0.02	1.74	1.99	0.02	0.06	1.21	2.36	2.44	1.35	2.20	2.15
Lu	0.04	0.00	0.27	0.32	0.00	0.01	0.19	0.40	0.42	0.25	0.35	0.35

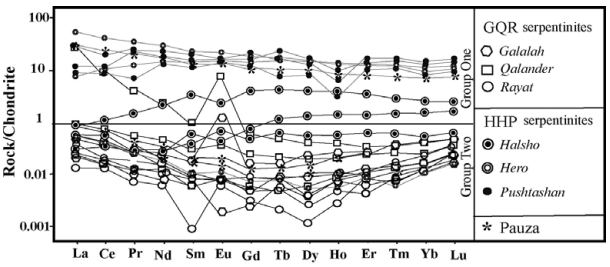

Figure 6. Chondrite-normalized REE diagram of all datasets. Note that analyses for this and subsequent diagrams have not been recalculated on an anhydrous basis.

GQR serpentinites are interpreted to be related, LREE-enhancing serpentinization processes (Niu, 2004). The absence of Ce anomalies in the REE plot may suggest that seawater effects on serpentinization processes were negligible (Niu & Hekinian, 1997). The REE patterns displayed by this group of samples are strictly related to Group Two (Fig. 6). Worth noting is that the REE patterns of the GQR serpentinites differ significantly from those of the HHP serpentinite–matrix mélange, which are either equally divided between the two REE patterns groups (Hero and Halsho) or inclined towards Group One (e.g. Pushtashan) (Fig. 7). The obvious differences between GQR and HHP serpentinite–matrix mélanges might be related to the evolution of the Zagros Suture Zone.

4.b. Normalized multi-element diagrams

The distinct differences between Group One and Group Two are graphically displayed in multi-element variation diagrams (spider diagrams) of all datasets, in which the trace elements are arranged in order of decreasing incompatibility from left to right, and normalized to the N-MORB source mantle concentrations of Sun & McDonough (1989). Bulk-rock MORB-normalized profiles of Group Two are almost flat in the MREE–HREE region with the flattening of profiles in the Gd–Lu range (> 3 times MORB composition). Compared with Group One, Group Two has extremely high content of REEs, displaying variable depletions in the moderately incompatible high-field-strength elements (HFSE) (Zr, Hf, Y) relative to their adjacent REEs (Fig. 8). Notable differences in the Group One spider diagram patterns (Figs 9, 10) include: (1) Large-ion lithophile element (LILE) and LREE values are notably lower for samples HS8 and HR25 with a Zr negative anomaly compared with HR18 and PZ9; (2) The spider diagrams show a significant negative Pb anomaly for all samples, with relatively flat patterns in the HFSEs; (3) PZ9 and HR18 show indistinguishable spider diagram patterns in which Cs, Rb, Nb, Pb and Nd negative anomalies are observed. The low variations in Cs, Rb and Pb concentrations and the 'spiky' LILEs indicate interaction with hydrothermal fluids and mobility of these trace elements during

https://doi.org/10.1017/S0016756811000409 Published online by Cambridge University Press

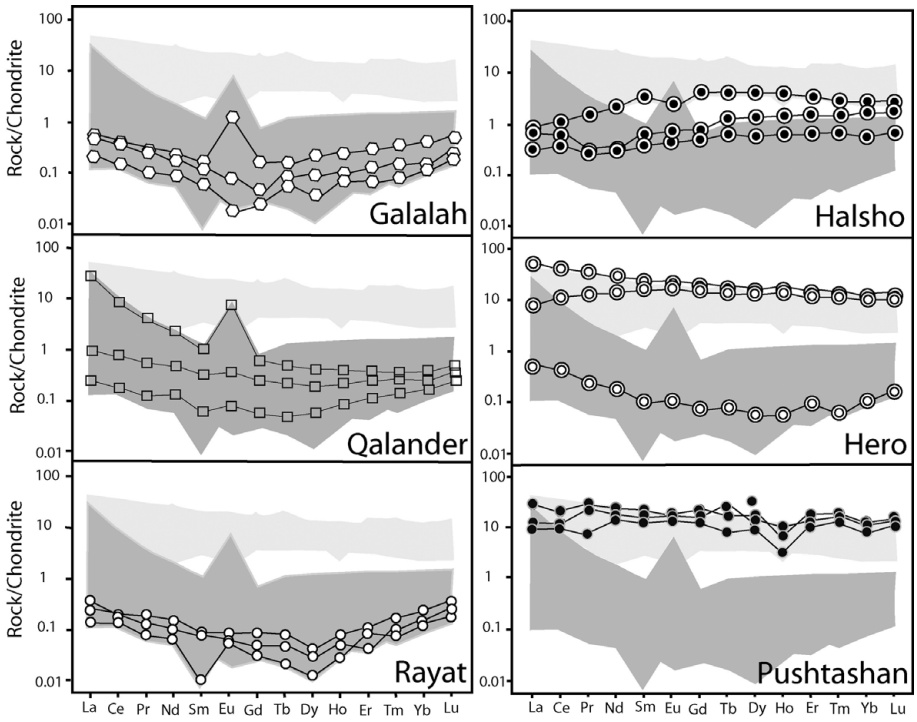

Figure 7. Chondrite-normalized REE diagram for the serpentinites studied classified according to their locality: GQR (Galalah, Qalander and Rayat) and HHP (Hero, Halsho and Pushtashan) serpentinite–matrix mélanges (Group One – light grey and Group Two – dark grey).

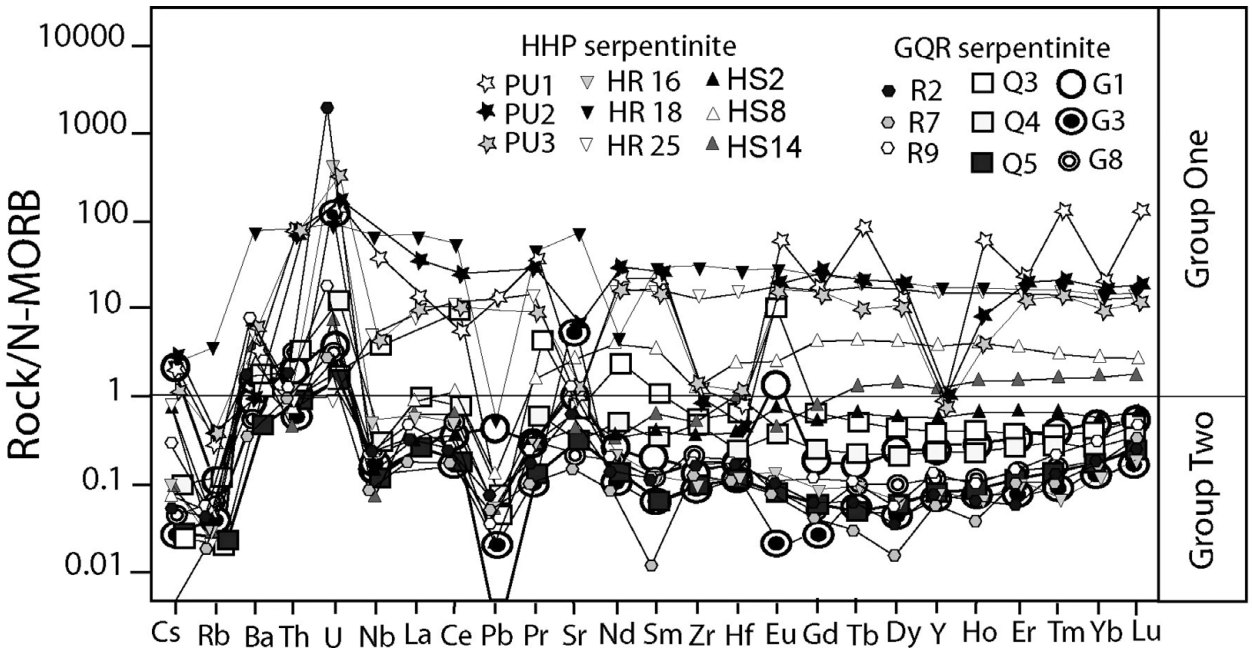

Figure 8. A multi-element spider diagram, normalized against N-MORB of all datasets. Values of normalizing constants are from Sun & McDonough (1989). Elements arranged in order of increasing compatibility (Hofmann, 1988). Sample numbers referred to in the inset are classified by locality: PU – Pushtashan; HR – Hero; HS – Halsho; R – Rayat; Q – Qalander; G – Galalah.

serpentinization; (4) The HR25 sample shows clear negative anomalies for Th, U and Sr. There are lower REE contents with flatter REE patterns (lower La/Yb ratios) in HS8 typical of cumulate gabbros, or otherwise mechanical mixing between gabbroic (and/or sedimentary) blocks and serpentinized tectonic matrix. High LREE/MREE ratios are displayed by HR18 and PZ9 in comparison to normal MORB. This shows that these rocks were already changed by additions from the subducted slab, although some characteristics of MORB (e.g. low LREE/MREE ratio) are still preserved in HR25 and HS8. The tectonic environment of this group is clear from the spider diagram pattern, which reflects the MORB source varying between N-MORB sources (HS8) and T-MORB or E-MORB sources for the other samples. In fact, hydration/dehydration

https://doi.org/10.1017/S0016756811000409 Published online by Cambridge University Press

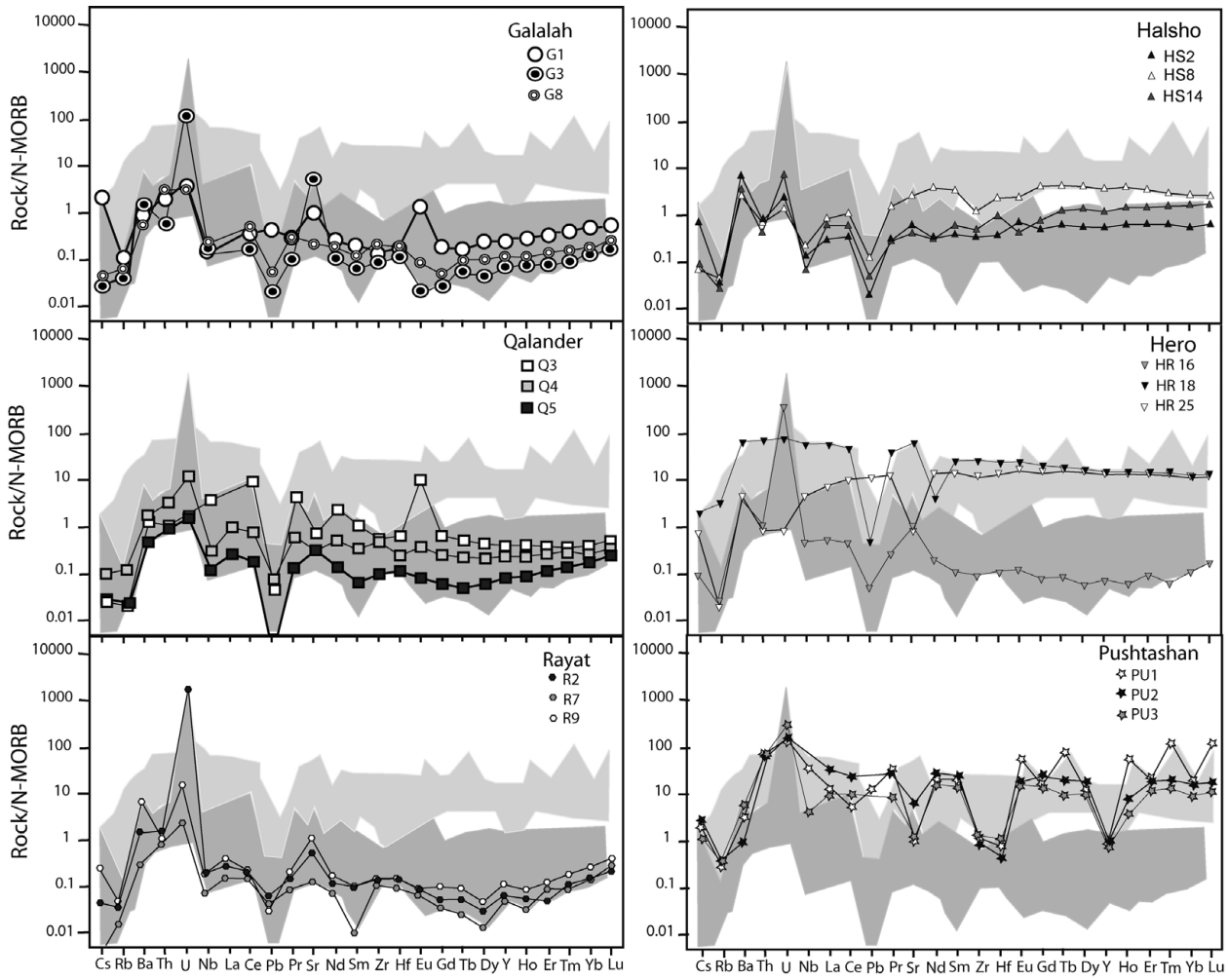

Figure 9. Multi-element spider diagram normalized against N-MORB of GQR and HHP serpentinite–matrix mélanges. Values of normalizing constants are from Sun & McDonough (1989). Elements arranged in order of increasing compatibility (Hofmann, 1988). Light and dark grey represent Group One and Group Two, respectively.

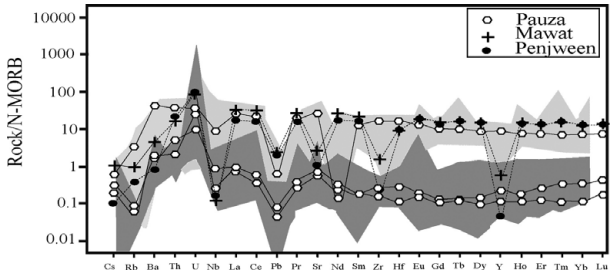

Figure 10. Multi-element spider diagram normalized against N-MORB of serpentinites associated with ophiolite massif. Note that PZ9 (Pauza Gp 1) displays low MgO < 10 %, which is not typical mélange serpentinite (i.e. broken formation. See text for more information). Group One – light grey and Group Two – dark grey. Note changes in HFSE depletion with concomitant changes in REE.

experiments (e.g. You *et al*. 1996; Kogiso, Tatsumi & Nakano, 1997) under both shallow and relatively deep subduction zone conditions demonstrate consistently that Nb, Zr–Hf are essentially immobile. The above reasoning suggests that the distinct negative anomalies in Nb, Zr and Hf relative to their adjacent REEs, which are displayed by a few samples of Group One (i.e. Mawat M7 and Penjween PN1, Fig. 10), indicate higher partition coefficients of the residual phases (i.e. retention of Nb, Zr and Hf in the residual HFSE-rich titanites?). The sources of these serpentinites appear to record the addition of Nb- and Zr–Hf-depleted silicate melts, possibly derived from subducted slabs, to a depleted mantle protolith. They are consistent with an important role for residual rutile. The data, and the spatial relationships of M7 and PN1, indicate a NW–SE chemical variation in serpentinites (i.e. GQR through HHP towards the Mawat–Penjween ophiolite massifs), owing to differences in source terrane, and in the processes that transported them into the mélange via subducted slabs.

5. Constraints from Th/La, U/La and Ba/Th ratios on sediment recycling in subduction zones

Mélange formed through the synergistic effects of deformation and metasomatic fluid flow affecting peridotite, basaltic and sedimentary protoliths to form hybridized bulk compositions, are not typical of

https://doi.org/10.1017/S0016756811000409 Published online by Cambridge University Press

seafloor 'input' lithologies. Geochemical investigations might suggest that the mélange studied contains heterolithic, chaotic subducted slabs incorporated into a serpentinite matrix. The latter, however, preserves no primary silicate minerals. The relics of unaltered primary Cr-spinel may provide useful petrogenetic information on the serpentinite matrix. This is because it maintains its compositional signature after serpentinization (N. Aziz, unpub. Ph.D. thesis, Sulaimani Univ., 2008). Hence, the composition of primary Cr-spinels of the studied serpentinites indicates that much of the serpentinite matrix appears to be derived from harzburgite and lherzolite of fore-arc affinity (Aswad *et al*. unpub. data, 2011). Mantle metasomatism by influx of subduction-derived components is the essential event resulting in enriched mantle wedge materials. The components derived from dehydration of a subducting slab are highly variable and include hydrous fluids/melts (e.g. Plank & Langmuir, 1993; Stern *et al*. 2006). Type of metasomatic agent (e.g. hydrous fluids or melts) and degree of metasomatism may lead to distinct chemical variations in mantle wedge material. For instance, elevated ratios of Ba/Th (1–1200), U/Th (0.04–90), Ba/La (1–285), Sr/Ce (0–422) and Ba/Rb (1–125) infer such metasomatism of their mantle source by slab-derived hydrous fluids. Th/Nb, also taken as an index of sediment melting by Elliott *et al*. (1997), varies in the serpentinites studied from 0.09 to 75. This is an order of magnitude higher than the Th/Nb of ~ 0.05 for MORB and is also significantly higher than the Th/Nb of ~ 0.24 for subducted sediment. Note that rutile as a residual phase accounts for the depletion of Nb, Ta and Ti in the melt. Therefore, the high Th/Nb and low Nb/La and Zr/Sm ratios appear to record the addition of Nb- and Zr–Hf-depleted silicate melt interacting with the overlying mantle wedge. The high Ba/Th, low La/Sm ratios (Fig. 11) (HS2; Ba/Th = 1200; La/Sm = 20) represent mantle modified by fluids from altered oceanic crust.

In speculation on the origins of the subducted sediments incorporated into a serpentinite matrix, ratio plots such as the U/La and Ba/Th plot are used (Fig. 12). The subducted sediments in the area studied contain hemipelagic and carbonate components (i.e. Qulqula Radiolarite and Balambo limestone). By arranging the elements in order of their overall hemipelagic/carbonate ratio (U, Cs, Th, K, Pb, La, Y, Ba, Sr), it become clear that U/La and Ba/Th ratios provide maximum separation between the hemipelagic and carbonate components (Patino, Carr & Feigenson, 2000). Ba/Th is exceptionally enriched in the carbonate section and provides a first-order tracer of the carbonate sediments. U/La is similar in MORB and carbonates but much higher in hemipelagic sediments. Therefore, U/La is used to track the hemipelagic sediment signal, whereas Ba/Th tracks the carbonate sediment signal. Wide separation of the fluid and melt compositions in a U/La versus Ba/Th diagram creates diagnostic mixing curves with an E-MORB source. Fluid from mature oceanic crust has high U/La, fluid from carbonate

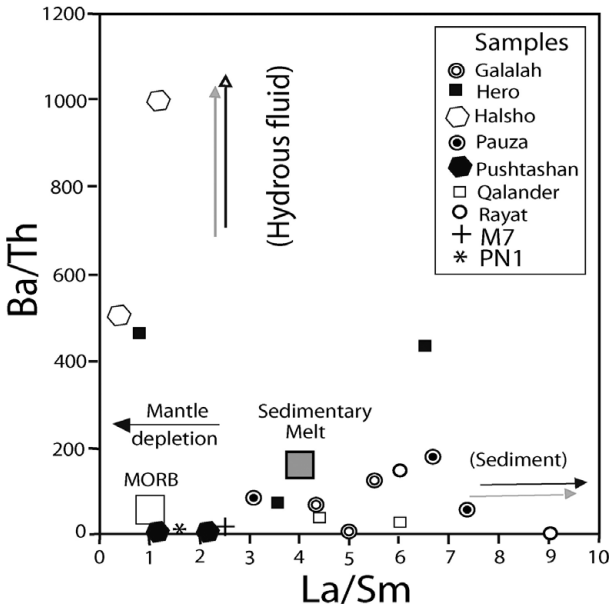

Figure 11. Ba/Th v. La/Sm of the studied serpentinites. Halsho serpentinites display higher Ba/Th and lower La/Sm ratios than the remaining samples, implying that the hydrous fluid influx had more influence on the serpentinization processes. These changes in Ba/Th and La/Sm ratios are likely to be a response to a gradual change in the influence of slab-derived fluids v. bulk sediment or sediment–melt involvement in serpentinite genesis.

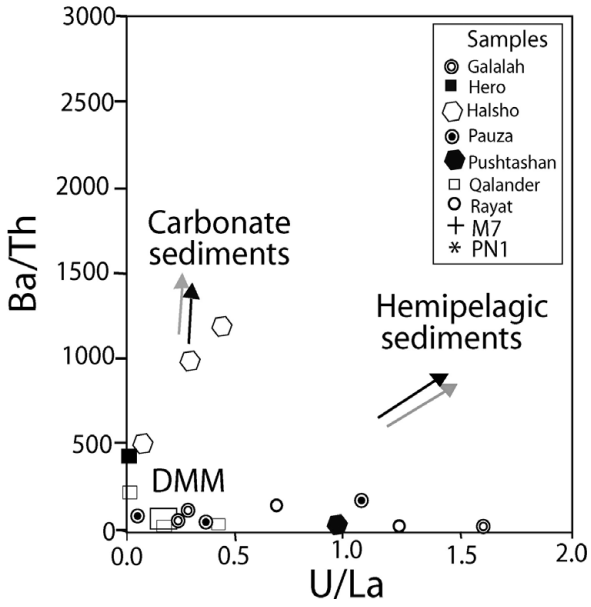

Figure 12. Ba/Th v. U/La. Halsho serpentinites display higher Ba/Th and lower U/La ratios than the remaining samples, implying that carbonate sediment has more influence on the serpentinization processes. Carbonate and hemipelagic sediments are from the DSDP (Deep Sea Drilling Project) (Patino, Carr & Feigenson, 2000).

sediment has high Ba/Th, and fluid and melt from hemipelagic sediments both have high U/La and Ba/Th. Halsho serpentinites (i.e. HS18, HS2 and HS8) have high Ba/Th and low U/La, whereas Rayat (R2 and R9) serpentinites tend to have high U/La and low Ba/Th (Fig. 12). The high Ba/Th of Halsho serpentinites imply that carbonate sedimentary components have had

https://doi.org/10.1017/S0016756811000409 Published online by Cambridge University Press

more influence on the mélange-forming processes. By employing a binary mixture of U/La values between the mantle (0.190) and the hemipelagic sediments (3.085), the tectonic signature of the serpentinite was distinguished from any sedimentary signature. The larger hemipelagic sediment contribution is only observed in the sample G3 from Galalah (1.6) ($\approx 49\,\%$ hemipelagic sediment). Otherwise, all the studied serpentinite 'mélanges' are tectonic in nature.

6. Tectonic implications

The serpentinite–matrix mélange of the Zagros Suture Zone represents an oceanic subduction channel related to Mesozoic subduction. This provides evidence for a long history of subduction, accretion, mélange formation and uplift. Study of major and trace elements shows that the exhumation of subducted components in the serpentinite–matrix mélange must have been accompanied by chemical interaction with serpentinites along the entire retrograde path. The data and the spatial relationships of the rocks studied ascribe a NW–SE chemical variation in serpentinites to differences in source terrane and in the processes that transported them into the mélange channel. This is confirmed through the changes in Ba/Th and La/Sm ratios, which are likely to be a response to a gradual change in the influence of slab-derived fluids versus bulk sediment or sediment–melt involvement in the serpentinite genesis. The thickness of the Lower Allochthon decreases considerably from northwest to southeast. For that reason, GQR and HHP serpentinite–matrix mélanges can only be distinguished in the northern part of the studied area. The prevalent view is that during a period of oceanic subduction (Late Cretaceous), the oceanic crust, the overlying sediments (i.e. hemipelagic sediment of Qulqula) and serpentinized peridotite from the overlying mantle wedge, part of which can be decoupled from the crust and accreted to form the accretionary wedge, were pulled at depth along the subduction zone into the subduction channel (e.g. Gerya & Stöckhert, 2002). The GQR serpentinite–matrix mélanges were unroofed by erosion during subduction at the end of Maastrichtian time. Field evidence based on Paleocene–Eocene arc activity (i.e. Walash volcanites, 43–32 Ma), suggests that the occurrence of these clasts of serpentinite–matrix mélanges in the Tanjero flysch (Maastrichtian age) does not necessarily constrain the end of subduction (Fig. 13). The emplacement of the serpentinite–matrix mélanges is more likely to have taken place before the resorption of the oceanic lithosphere. The average upward velocity of serpentinite depends on the width of the subduction channel, the viscosity of serpentinite (and hemipelagic sediment associates) and the dip angle of subduction (Horodyskyj, Lee & Luffi, 2009). The average net upward velocity is the difference between the upward channel velocity and the downward-sinking velocity of the slab. The latter is a function of the relative plate velocity and β, which is the angle of oblique convergence (0° reflects pure normal convergence and 90° represents pure strike-slip motion) (Horodyskyj, Lee & Luffi, 2009). Based on the data obtained from six GPS receiving stations of the Iraqi Geospatial Reference System (IGRS) (Kadir, unpub. Ph.D. thesis, Mosul Univ., Iraq, 2008), the angle of oblique convergence (β) in the studied area ranges between 47° and 50° NW with a relative plate velocity of 35 mm yr^{-1}. The occurrence of two magma series in the Walash volcano-sedimentary sequences (i.e. basaltic and andesitic series; A. Koyi, unpub. M.Sc. thesis, Mosul Univ. Iraq, 2006) in a single volcanic edifice could be equally formed during metasomatism of the pre-existing mantle wedge by either the supercritical melt (Stage I) or aqueous fluid (Stage II) released by the subducted slab of the Arabian plate, which dipped at a high angle ($\sim 70°$). The high-angle dip is characterized by the occurrence of two magma series in the Walash volcano-sedimentary sequences (i.e. basaltic and andesitic series; A. Koyi, unpub. M.Sc. thesis, Mosul Univ. Iraq, 2006) from a single volcanic edifice (Fig. 14).

Increasing field-based evidence for the involvement of serpentinized peridotite from the overlying mantle wedge in the subduction channel (Hermann, Miintener & Scambelluri, 2000; Schwartz *et al*. 2001) indicates that this channel could have played a major role in subduction dynamics down to depths limited only by the stability of serpentine minerals (Wunder, Baronnet & Schreyer, 1997; Schmidt & Poli, 1998). The serpentinite channel could represent a convenient exhumation pathway for subducting components. Serpentinite has a much lower density than the mantle (2700 kg/m^3 compared to 3300 kg/m^3) and very low viscosity (Hilairet *et al*. 2007). The former provides a strong buoyancy force generating a pressure gradient that can drive the serpentinite to the surface, whereas the low viscosity reduces the viscous resisting forces (Ernst, Maruyama & Wallis, 1997; Guillot *et al*. 2001). Coupled with erosion of the serpentinite at the surface, considerable upward transport along this serpentine channel may occur. It is important that there is a relationship between the thickness of the serpentinite (and hemipelagic sediments) and the ascent rate, because the thinner the layer the greater the viscous resisting forces and the slower the ascent rate. Thus, large layer thicknesses are needed for mélange ascent rates to exceed the downward pulling force associated with the subducting slab (layer thicknesses must be > 10 km for a ~ 10 cm yr^{-1} plate velocity (Schwartz *et al*. 2001). The rocks locally exhibit the block-in-matrix structure of accretionary mélanges, with a combination of metamorphosed oceanic crust fragments, dismembered ophiolites and sedimentary exotic blocks in serpentinite matrix. With this in mind the strength of serpentinite mélange might differ owing to the existence of variable amount of exotic blocks in the block-in-matrix structure or bimrock (Lindquist & Goodman, 1994). Given the configuration stated above, which is based on the coexistence of intraoceanic

https://doi.org/10.1017/S0016756811000409 Published online by Cambridge University Press

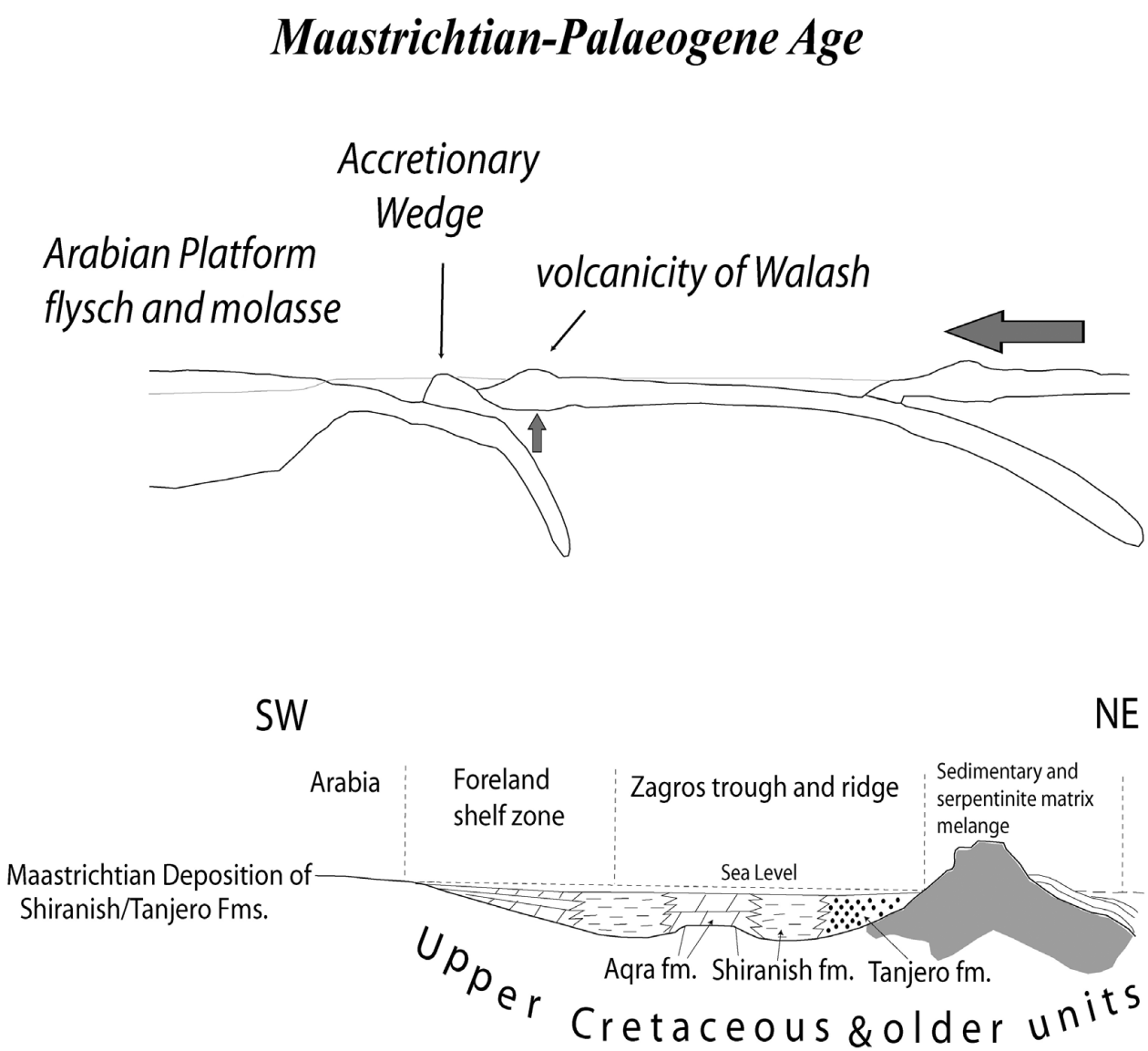

Figure 13. Sketch showing the tectonic evolution of the proto-foreland basin of the Kurdish Zagros Suture Zone (KZSZ) (Maastrichtian–Palaeogene).

subduction types, the early tectonomagmatic episode is considered to be related to the closure of the Tethys Ocean, which culminated in two subduction types (Aswad, 1999). It is assumed here that this tectonic regime was activated by a high converging velocity (Agard *et al*. 2007), which caused stresses to accumulate in the oceanic lithosphere leading to the formation of an additional subduction of the oceanic crust away from the Neo-Tethyan palaeo-ridge or proximal to the Arabian platform. The volcanic units of the Gemo Group (Albian–Cenomanian), which are dominated by boninitic volcanism (Farjo, unpub. M.Sc. thesis, Mosul Univ. Iraq, 2006), overlie the uppermost part of the Mawat ophiolitic sequence. These rock units with their arc signature strongly suggest an infant-arc subduction of Albian–Cenomanian age (97–118 Ma; Aswad & Elias, 1988). Based on ophiolite mantle flow structures, a number of authors have proposed that subduction was initiated at the locus of the Neo-Tethyan palaeo-ridge (Nicolas, 1989; Boudier & Nicolas, 1988; Nicolas *et al*. 2000). The infant-arc episode was followed by at least two further episodes of orogenic activity impacting the Neo-Tethyan margin prior to its final incorporation into the Arabian plate (see for example, Aswad, 1999). The Late Cretaceous, however, saw a radiolarite rise coupled with a flysch basin on its inboard side. The facies changes were probably triggered by plate convergence incipient in the early Campanian (first episode) and continuing through the Palaeogene period (second episode), where the volcanic flysch and nummulite carbonates were still accumulating on the remaining oceanic lithosphere. The Qulqula Radiolarite Formation, which apparently records deposition in a deep marine setting distal to the Arabian continental margin (and serpentinite mélange), was removed from the subducting plate and accreted against the overriding plate forming an accretionary wedge, which marks the transition from passive margin to the foreland basin setting (Fig. 15). Deformation of the Arabian platform flysch is much slower than that of

https://doi.org/10.1017/S0016756811000409 Published online by Cambridge University Press

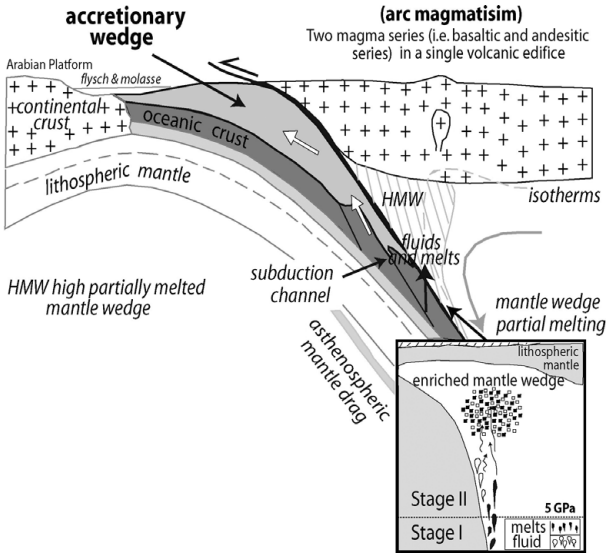

Figure 14. Tectonic model of accretion of Qulqula Radiolarite and GQR serpentinite–matrix mélanges onto the Arabian continental margin through Maastrichtian–Palaeogene time.

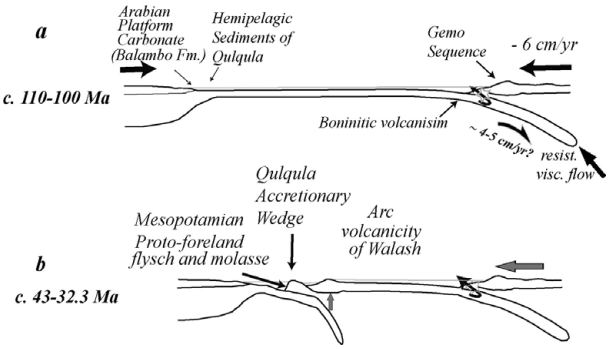

Figure 15. Postulated tectonic evolution model for the Kurdish Zagros Suture Zone (KZSZ) during late-Mesozoic to mid-Palaeogene time. See text for discussion.

the accreted sediments. High-degree deformation of the latter was attained during exhumation as a consequence of the development of an accretionary prism related to the late subduction. This tectonic episode may have been caused by abrupt increases in the convergence rates from *c*. 2–3 cm yr^{-1} to 6 cm yr^{-1} as a result of worldwide intraplate instabilities in response to superplume events (Agard *et al*. 2007). The time lapse between the velocity increase and the initiation of subduction (105 ± 5 Ma; Aswad & Elias, 1988) is estimated at over 20 Ma, and would correspond to the time necessary for the build-up of an accretionary wedge and for rupture of the oceanic lithosphere. This short-term variation in the convergence rate was responsible for creation of a new intraoceanic subduction zone, culminating in the Palaeogene arc volcanicity of Walash (43.1 ± 0.3–32.3 ± 0.4 Ma, Middle Eocene–Late Eocene) (A. Koyi, unpub. M.Sc. thesis, Mosul Univ. Iraq, 2006). Therefore, the final resorption of the oceanic domain must have taken place slightly after 32.3 Ma followed by collision. This proposed model, however, predicts fast exhumation velocities for the hemipelagic sediments and the oceanic crust (> 1 cm yr^{-1}). The sediments are efficiently decoupled from the oceanic crust and tend to accumulate in the accretionary wedge (Qulqula rise). Further to the east of the Qulqula rise, however, a Neo-Tethyan strand remained open into the Palaeogene, following major ophiolitic serpentinite mélange emplacement.

7. Conclusions

Geochemical analysis in combination with geological observations allows the following conclusions:

(1) There are two types of serpentinite: (1) serpentinite imbricates and (2) serpentinite–matrix mélanges. The first type, which is associated with ophiolites, includes serpentinite broken formation (massive blocks of metabasite enclosed in a matrix of serpentinite schist) of 80–110 Ma. The second type of serpentinite has drastically different petrogenesis, age and regional field relationships, consists of exotic blocks of mixed age (150–200 Ma) and possesses εNd(i) down to −30 (Aziz, Elias & Aswad, 2011).

(2) Unlike the serpentinites associated with the ophiolites, serpentinite–matrix mélange defies a simple geochemical categorization. It was formed through the synergistic effects of deformation and metasomatic fluid flow affecting peridotite, basaltic and sedimentary protoliths to form hybridized bulk compositions.

(3) Based on the available geological and tectonic setting criteria, the serpentinite–matrix mélanges are subdivided into: (1) HHP (Hero, Halsho, Pushtashan) serpentinite–matrix mélange and (2) GQR (Galalah, Qalander and Rayat) serpentinite–matrix mélange.

(4) The overall chondrite-normalized REE patterns of the serpentinites display significant REE variability and are divided into two main groups: Group One (i.e. > 1 × chondrite) and Group Two (i.e. < 0.01 to 1 × chondrite). This implies different origins.

(5) GQR serpentinite–matrix mélanges have a noticeably high LREE and positive Eu anomaly. Their HREEs never reach more than 1 × chondrite (CI) (i.e. < 0.01 to 1 × chondrite) and they are allotted to Group Two. The HHP serpentinite–matrix mélanges are either equally divided between the two REE pattern groups (e.g. Hero, Halsho) or inclined towards Group One (e.g. Pushtashan)

(6) Plots of the U/La and Ba/Th ratios suggest that subducted sediments (i.e. Qulqula Radiolarite and Balambo limestone?) were consecutively incorporated into a serpentinite–matrix mélange.

(7) The influx of subducted components into the mantle wedge relies heavily on the composition of the sedimentary inputs, which varies considerably with time from hemipelagic (Qulqula Radiolarite) to carbonate sediments (Balambo limestone).

(8) Based on field evidence, it is concluded that the GQR and HHP serpentinite–matrix mélanges were emplaced in late Maastrichtian and late Palaeogene time, respectively.

https://doi.org/10.1017/S0016756811000409 Published online by Cambridge University Press

References

AGARD, P., JOLIVET, L., VRIELYNCK, B., BUROV, E. & MONIÉ, P. 2007. Plate acceleration: the obduction trigger? *Earth and Planetary Science Letters* **258**, 428–41.

ASWAD, K. J. 1999. Arc–continent collision in northeastern Iraq as evidenced by Mawat and Penjwin Ophiolite Complexes. *Raffidain Journal of Science* **10**, 51–61.

ASWAD, K. J. A., AZIZ, N. R. H. & KOYI, H. A. 2011. Cr-spinel compositions in serpentinites and their implications for the petrotectonic history of the Zagros Suture Zone, Kurdistan Region, Iraq. *Geological Magazine*, doi: 10.1017/S0016756811000422.

ASWAD, K. J. & ELIAS, E. M. 1988. Petrogenesis, geochemistry and metamorphism of spilitized subvolcanic rocks of the Mawat Ophiolite Complex, NE Iraq. *Ofiolitti* **13**, 95–109.

AZIZ, N. R. H., ELIAS, E. M. & ASWAD, K. J. 2011. Rb–Sr and Sm–Nd isotope study of serpentinites and their impact on the tectonic setting of Zagros Suture Zone, NE-Iraq. *Iraqi Bulletin of Geology and Mining* **7**, 67–75.

BOUDIER, F. & NICOLAS, A. (eds). 1988. Special Issue: The Ophiolites of Oman. *Tectonophysics* **151**, 1–401.

ELLIOTT, T., PLANK, T., ZINDLER, A., WHITE, W. & BOURDON, B. 1997. Element transport from slab to volcanic front at the Mariana arc. *Journal of Geophysical Research* **102**, 14991–15019.

ERNST, W. G., MARUYAMA, S. & WALLIS, S. 1997. Buoyancy-driven, rapid exhumation of ultrahigh-pressure metamorphosed continental crust. *Proceedings of the National Academy of Sciences of the United States of America* **94**, 9532–7.

GERYA, T. V. &. Stöckhert, B. 2002 Exhumation rates of high pressure metamorphic minerals in subduction channels: the effect of rheology. *Geophysical Research Letters* **29**, 1261, doi: 10.1029/2001GL014307, 4. pp.

GOVINDARAJU, K. 1995. 1995 working values with confidence limits for twenty-six CRPG, ANRT and IWG-GIT geostandards. *Geostandards Newsletter* **19** (Special Issue), 1–32.

GUILLOT, S., HATTORI, K. H., DE SIGOYER, J., NAGLER, T. & AUZENDE, A.-L. 2001. Evidence of hydration of the mantle wedge and its role in the exhumation of eclogites. *Earth Planetary Science Letters* **193**, 115–27.

HERMANN, J., MIINTENER, O. & SCAMBELLURI, M. 2000. The importance of serpentinite mylonites for subduction and exhumation of oceanic crust. *Tectonophysics* **327**, 225–38.

HILAIRET, N., REYNARD, B., WANG, Y., DANIEL, I., MERKEL, S., NISHIYAMA, N. & PETITGIRARD, S. 2007. High pressure creep of serpentine, interseismic deformation, and initiation of subduction. *Science* **318**, 1910–13.

HOFMANN, A. W. 1988. Chemical differentiation of the earth: the relationship between mantle, continental crust, and oceanic crust. *Earth and Planetary Science Letters* **90**, 297–314.

HORODYSKYJ, U., LEE, C. T. A. & LUFFI, P. 2009. Geochemical evidence for exhumation of eclogite via serpentinite channels in ocean-continent subduction zones. *Geosphere* **5**, 426–8.

JASSIM, S. Z. & BUDAY, T. 2006. Units of the unstable shelf and the Zagros Suture, Chapter 6. In *Geology of Iraq* (eds S. Z. Jassim & J. C. Goff), pp. 71–90. Brno, Czech Republic: Dolin, Prague and Moravian Museum.

JASSIM, S. Z., SUK, M. & WALDHAUSROVA, J. 2006. Magmatism and metamorphism in the Zagros Suture, Chapter 17. In *Geology of Iraq* (eds S. Z. Jassim & J. C. Goff), pp. 212–31. Brno, Czech Republic: Dolin, Prague and Moravian Museum.

KING, R. L., BEBOUT, G. E., MORIGUTI, T. & NAKAMURA, E. 2006. Elemental mixing systematics and Sr-Nd isotope geochemistry of mélange formation: obstacles to identification of fluid sources to arc volcanics. *Earth and Planetary Science Letters* **246**, 288–304.

KOGISO, T., TATSUMI, Y. & NAKANO, S. 1997. Trace element transport during dehydration processes in the subducted oceanic crust: 1. Experiments and implications for the origin of ocean island basalts. *Earth and Planetary Science Letters* **148**, 193–205.

LINDQUIST, E. S. & GOODMAN, R. E. 1994. The strength and deformation properties of a physical model melange. In *Proceedings of the first North American Rock Mechanics Symposium (Narms) (Austin, Texas)*: (eds P. P. Nelson & S. E. Laubach), pp. 843–50. Rotterdam: A.A. Balkema.

LIU, X. & O'NEILL, H. STC. 2000. The effect of Cr_2O_3 on partial melting relations in the model mantle system CMAS-Cr_2O_3. In *Australian National University Research School of Earth Sciences Annual Report 2000*, pp. 104–5.

NIU, Y. 2004. Bulk-rock major and trace element compositions of abyssal peridotites: implications for mantle melting, melt extraction and post-melting processes beneath mid-ocean ridges. *Journal of Petrology* **45**, 2423–58.

NIU, Y. & HEKINIAN, R. 1997. Basaltic liquids and harzburgitic residues in the Garrett Transform: a case study at fast-spreading ridges. *Earth and Planetary Science Letters* **146**, 243–58.

NICOLAS, A. 1989. *Structures of ophiolites and dynamics of oceanic lithosphere*. Dordrecht: Kluwer Academic, 368 pp.

NICOLAS, A., ILDEFONSE, B. BOUDIER, F., LENOIR, X. & BEN ISMAIL, W. 2000. Dike distribution in the Oman-United Arab Emirates ophiolite. *Marine Geophysical Researches* **21**, 269–87.

PATINO, L. C., CARR, M. J. & FEIGENSON, M. D. 2000. Local and regional variations in Central American arc lavas controlled by variations in subducted sediment input. *Contributions to Mineralogy and Petrology* **138**, 265–83.

PLANK, T. & LANGMUIR, C. H. 1993. Tracing trace elements from sediment input into volcanic output at subduction zones. *Nature* **362**, 739–42.

SALTERS, V. J. M., LONGHI, J. E. & BIZIMIS, M. 2002. Near mantle solidus trace element partitioning at pressures up to 3.4 GPa. *Geochemistry, Geophysics, Geosystems (G^3)* **3**, 1038, doi:10.1029/2001GC000148, 23 pp.

STERN, R. J., KOHUT, E. J., BLOOMER, S. H., LEYBOURNE, M., FOUCH, M. & VERVOOT, J. 2006. Subduction factory processes beneath the Guguan cross-chain, Mariana Arc: no role for sediments, are serpentinites important? *Contributions to Mineralogy and Petrology* **151**, 202–21.

SCHMIDT, M. W. & POLI, S. 1998. Experimentally based water budgets for dehydrating slabs and consequences for arc magma generation. *Earth and Planetary Science Letters* **163**, 361–79.

SCHWARTZ, D. P., STENNER, H. D., COSTA, C., SMALLEY, R., ELLIS, M. & VELASCO, M. 2001. Paleoseismology at the end of the world: initial observations of the Fagnano Fault, Tierra Del Fuego, Argentina. *Seismological Research Letters* **72**, 265.

SUN, S. S. & MCDONOUGH, W. E. 1989. Chemical and isotopic systematics of ocean basalt: implications for mantle composition and processes. In *Magmatism in the Ocean Basins* (eds A. D. Saunders & M. J. Norry), pp. 313–45. Geological Society of London, Special Publication no. **42**.

WUNDER, B., BARONNET, A. & SCHREYER, W. 1997. Ab-initio synthesis and TEM confirmation of antigorite in the system MgO-SiO_2-H_2O. *American Mineralogist* **82**, 760–4.

YOU, C.-F., CASTILLO, P. R., GIESKES, J. M., CHAN, L. H. & SPIVACK, A. J. 1996. Trace element behavior in hydrothermal experiments: implications for fluid processes at shallow depths in subduction zones. *Earth and Planetary Science Letters* **140**, 41–52.

https://doi.org/10.1017/S0016756811000409 Published online by Cambridge University Press